Application of Landsat ETM+ and OLI Data for Foliage Fuel Load Monitoring Using Radiative Transfer Model and Machine Learning Method

Xingwen Quan, Yanxi Li, Binbin He, Geoffrey J. Cary, and Gengke Lai

***Abstract*—Foliage fuel load (FFL) is a critical factor affecting crown fire intensity and rate of spread. Satellite observations provide the potential for monitoring FFL dynamics across large areas. Previous studies commonly used empirical methods to estimate FFL, which potentially lacks reproducibility. This study applied Landsat 7 ETM+ and 8 OLI data for FFL retrieval using radiative transfer model (RTM) and machine learning method. To this end, the GeoSail, SAIL, and PROSPECT RTMs were first coupled together to model the near-realistic scenario of a two-layered forest structure. Second, available ecological information was applied to constrain the coupled RTM modeling phases in order to decrease the probability of generating unrealistic simulations. Third, the coupled RTMs were linked to three machine learning models—random forest, support vector machine, and multilayer perceptron—as well as the traditional lookup table. Finally, the performance of each method was validated by FFL measurements from Southwest China and Sweden. The resulting multilayer perceptron ($R^2 = 0.77$, RMSE $= 0.13$, and rRMSE $= 0.43$) outperformed the other three methods. The evaluation of the applicability of the FFL estimates was conducted in a southwest China forest where two occurred in 2014 and 2020. The FFL dynamics from 2013 through 2020 showed that the fire was likely to occur when the FFL accumulated to a critical point (around 27×10^6 kg), highlighting the relevance of remote sensing derived FFL estimates for understanding potential fire occurrence.**

***Index Terms*—Fire, fire danger, foliage fuel load (FFL), forest, inversion, Landsat, machine learning method, radiative transfer model (RTM), remote sensing.**

Manuscript received October 28, 2020; revised January 9, 2021 and February 19, 2021; accepted February 19, 2021. Date of publication February 25, 2021; date of current version May 27, 2021. This work was supported in part by the National Natural Science Foundation of China under Contract 41801272 and Contract U20A2090, and in part by Sichuan Science and Technology Program under Contract 2020YFS0058. *(Corresponding author: Binbin He.)*

Xingwen Quan is with the School of Resources and Environment, University of Electronic Science and Technology of China, Chengdu 610054, China, and also with the Yangtze Delta Region Institute (Huzhou), University of Electronic Science and Technology of China, Huzhou 313001, China. (e-mail: xingwen.quan@uestc.edu.cn).

Yanxi Li, Binbin He, and Gengke Lai are with the School of Resources and Environment, University of Electronic Science and Technology of China, Chengdu 610054, China. (e-mail: 785825309@qq.com; binbinhe@uestc.edu.cn; laigengke@gmail.com).

Geoffrey J. Cary is with the Fenner School of Environment and Society, Australian National University, Canberra, ACT 2600, Australia. (e-mail: geoffrey.cary@anu.edu.au).

This article has supplementary material provided by the authors and color versions of one or more figures available at https://doi.org/10.1109/JSTARS.2021.3062073.

Digital Object Identifier 10.1109/JSTARS.2021.3062073

I. Introduction

Forest fires not only release considerable greenhouse gases, severely disturb the natural environment, but also pose a significant threat to people's lives and property [1], [2]. Forest fuel is a key variable affecting wildfire occurrence, spread, and intensity [3] and is commonly split into three classes: crown fuel, understory fuel, and surface fuel [4], [5]. Forest crown fires are typically of great concern since they are more difficult to control than surface fires, and their effects are more severe and long lasting [6]. Thus, crown fuel characteristics, which influence crown fire initiation, spread, and intensity [7]–[9], are of great interest to fire managers. Crown fuel commonly includes foliage, fine branch wood, and arboreal lichens and mosses[2], among which the foliage is the most flammable component [10]. Within this context, the foliage fuel load (FFL) can be regarded as a key fuel variable for crown wildfire danger assessment and typically refers to the dry weight of all tree canopy leaves (both dead and live) per unit area of the forest [11], [12]. Therefore, the accurate estimation and mapping of FFL can assist fire managers in optimizing prefire risk warnings and identification of safety zones for firefighters [8], [13].

The traditional fuel load (including FFL) acquisition involves destructive sampling. Although this approach is the most accurate, it is time-consuming, labor-intensive, and destructive with restricted application to large regions [8], [14], [15]. The fast-paced development of remote sensing techniques over the past two decades [2] provides great potential to estimate fuel load characteristics due to adequate spatiotemporal observation and multispectral information relating to leaf attributes, with the assessment of fuel loads in inaccessible terrain also possible [16]–[18].

A common method for remote sensing based fuel load estimation is to apply empirical methods that normally rely on linear or nonlinear relationships between the fuel load (or biomass) measurements and multisource remote sensing data (such as multispectral, radar, and light detection and ranging). These empirical formulae are straightforward and widely used and, therefore, have been applied for sensor-specific and site-dependent fuel load estimation [16], [19]–[28]. However, empirical methods typically lack reproducibility to be robustly applied to other areas [29].

Alternatively, the inversion of radiative transfer models (RTMs) can be used to derive biophysical and biochemical variables from remote sensing data. RTMs, such as scattering by arbitrarily inclined leaves (SAIL) [30], [31], GeoSail [32], and PROSPECT [33], were built based on physical laws that provide explicit relations between canopy or leaf properties and reflectance. Thus, RTM-based approaches have the advantage of being reproducible, with relevance to other sites and satellite sensors, for estimating the variables of interest at local to global scales [29], [34], [35]. Different strategies have been proposed for the inversion of these models, including numerical optimizations [36], [37], lookup tables (LUT) [38]–[40], and machine learning methods [41]–[43]. Each inversion method has advantages and disadvantages. Inverted parameters derived from numerical optimization approaches are of high precision but the method is slow, especially for complex models [44]. LUT algorithms are global optimization algorithms that are easily implemented and computationally efficient while retaining a relatively high precision for target variables. Therefore, this approach has been broadly used for the retrieval of vegetation canopy variables [45]. However, RTM inversions can be confounded since the measurements, model uncertainties, and different combinations of model parameters may correspond to almost identical reflectance [46], [47]. For this reason, previous studies also note that LUT inversion methods can generate diverse results [34], [38], [45], [48], [49].

Current popular machine learning methods, such as random forest (RF), support vector machine (SVM), and multilayer perceptron (MLP), involve automatically fitting parameters to observed data without prior knowledge or model calibration, theoretically supporting the application over large spatiotemporal scales [50]–[52]. An essential step for applying these methods is to train the models using samples from field measurements and satellite observations. However, adequate and extensive samples are required in this training process to avoid underfitting problems that dramatically decrease model robustness. To address this, earlier studies have linked RTM with machine learning methods [53]–[55] and apply this approach to retrieve biogeophysical parameters, including leaf area index (LAI) [42], [56], canopy water content (CWC) [43], crop primary productivity [57], and photosynthetically active radiation [58]. Despite this, the combined use of RTM with machine learning methods for FFL retrieval is still poorly developed.

Within this context, this study focused on the application of the Landsat 7 ETM+ and 8 OLI data for the FFL estimation by linking the RTM with the machine learning method. The performances of the FFL estimates were validated against measurements taken from southwest China and Sweden. The application value of this approach was explored by analyzing the relationship between the satellite-derived FFL dynamics and wildfire occurrences in a fire-prone region in southwest China. The overarching objective of this study is to test the feasibility of the satellite-derived FFL in fire management for crown fire risk assessment, suppression, and response.

II. Materials

A. Study Area and Field Measurements

Two study areas (see Fig. 1), the Vindeln (site 5, 64°14′N, 19°46′E) municipality in Västerbotten province of northern Sweden and a region in southwestern China, were selected to validate the FFL estimates. The first area is predominantly characterized by pine, spruce, and birch tree species with less aspen and other broadleaf tree types. A total of 10 circular sample plots (radius 10 m) were laid out in each of 31 stands to determine average tree diameter at breast height (DBH) for trees with DBH > 4 cm. The FFL was computed by Peterson's biomass functions with detailed methodology available in [59]. This dataset was provided by the European Space Agency Earth Observation campaigns.[1]

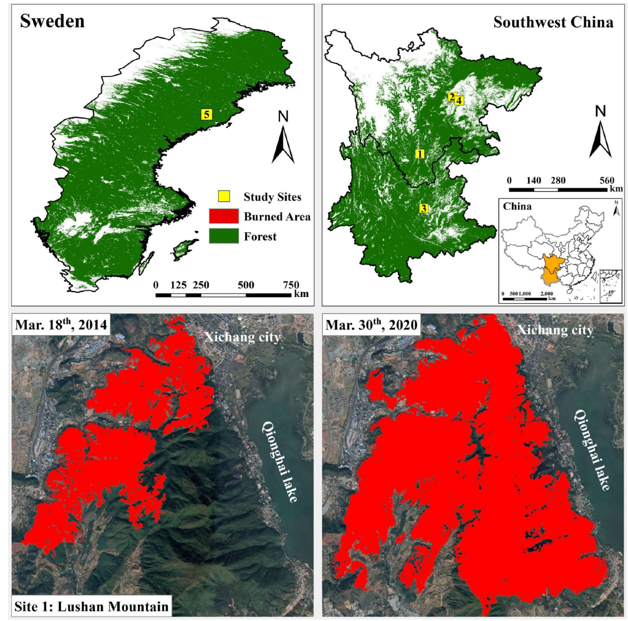

Fig. 1. Location of the study areas, including Sweden (upper left) and southwest China (upper right). A total of five study sites were selected, four in southwest China and one in Sweden. The bottom panels indicate the burned area of two wildfire events that occurred at Lushan Mountain (Site 1) on 18th March, 2014, and 30th March, 2020. The background image in the lower panels was downloaded from Google Earth.

For the southwestern China area, the forests can be roughly classified as evergreen broadleaf, broadleaved deciduous, and other pine species, such as the *Pinus Yunnanensis* and *Pinus Massoniana*. Due to the subtropical monsoon climate and geographic location, the forest ecosystem in this region typically has two canopy layers: an overstory tree canopy layer and an understory grass canopy layer. These forests have been historically vulnerable to wildfires, particularly in the last ten years.[2] For example, two wildfires occurred in the Lushan Mountain area (Site 1) on the 18th of March 2014 and the 30th of March 2020. The local government reported that these human-ignited fires were initially surface fires that subsequently ignited tree crowns. In addition to the climatic conditions, the large amount of crown fuel increased fire intensity leading to the fire becoming uncontrollable. The intense crown fire seriously hampered rescue and control, leading to the latter wildfire tragically causing the death of 19 firefighters.

Four study sites in the southwestern China area were sampled, including at Lushan Mountain (Site 1, 27°49′N, 102°15′E),

[1] [Online]. Available: http://eopi.esa.int

[2] [Online]. Available: http://web.sctjj.cn/tjcbw/tjnj/2019/zk/indexch.htm

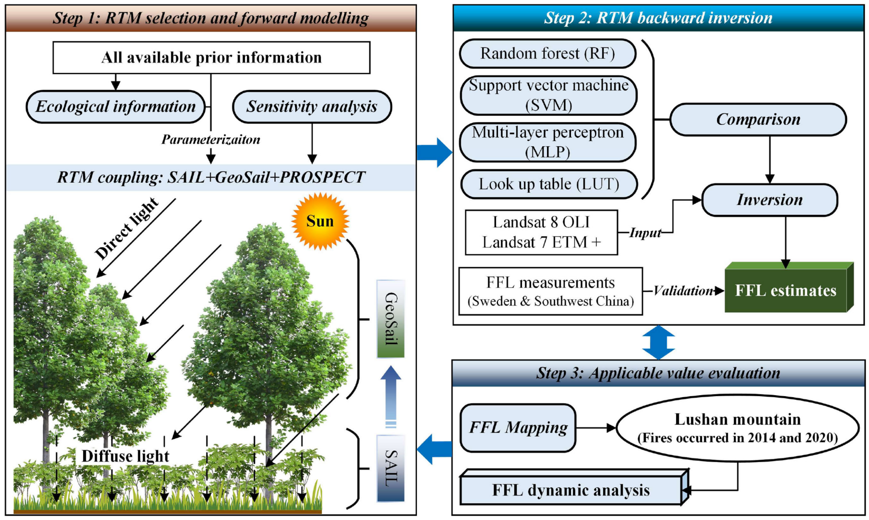

Fig. 2. Flowchart of the methodology for FFL retrieval by linking RTMs with machine learning methods.

Shiyuanbai Park (Site 2, 30°45′N, 103°55′E), Wenquan Town (Site 3, 24°59′N, 102°27′E), and Baigongyan Park (Site 4, 30°34′N, 104°17′E). The forests at sites 1, 3, and 4 are natural, while the vegetation at site 2 is planted. For these sites, the LAI of the tree canopy was measured using a fisheye camera system (Hemiview and EOS60D and Sigma EX DC4.5). Tree leaves (>120 g) were sampled using high branch scissors, while leaf area for all the leaves was measured using an LI-3000C leaf area meter. The leaf dry matter content (DMC, g/cm^2) was determined as the ratio of dry weight (oven dried for 48 h at 70 °C) and leaf area. A total of 41 plots were sampled between the 8th and 11th of April, 2015, at site 1. Six plots were sampled on the 24th June and 3rd July, 2020, at site 2, and ten plots were sampled on the 21st August, 2017, at site 4. The FFL measurements (kg/m^2) for these sites were derived as the product of total LAI and leaf DMC, i.e., total LAI (m^2/m^2) $\times$ DMC (g/cm^2) $\times$ 10. Here, the multiplier of ten is a coefficient that transfers the unit of DMC (g/cm^2) into kg/m^2. LAI was not measured for site 3, and therefore, the FFL was not available for this site. However, other information (DMC, leaf chlorophyll, species, etc.) from this site was used to regularize the RTM parameterization.

B. Satellite Data

The FFL data in Sweden were expressed for forest stands rather than a point scale measurement in the BIOSAR 2008 dataset. To match the Vindeln field data, a Landsat 7 ETM+ (07th October, 2008) product was acquired from the Google Earth engine (GEE) [60]. However, the ETM+ data collected after the 31st of May, 2003, exhibited gaps due to a problem in the scan line corrector system [61]. For those stands away from the gaps in Landsat 7 ETM+ data, all pixels in stands were extracted and averaged to represent the whole stand. For those stands partly located in the gaps, all pixels away from the data gaps in these stands were extracted and averaged. No stand was found wholly located in an ETM+ data gap. Given the impact of edge vegetation environments, ArcGIS (Version: 10.2) was used to generate a 10 m buffer around the inward edge of forest stand polygons to exclude edge pixels. For southwestern China sites, Landsat 8 OLI products were used, and two scenes were downloaded from GEE for Lushan Mountain (1st April, 2015, and 17th April, 2015), three for Baigongyan Park (5th August, 2017, 21st August, 2017, and 6th September, 2017), and one for Shiyuanbai Park (10th June, 2020). Each sample plot was matched with the relevant 3 $\times$ 3 satellite pixels, and the mean reflectance values for each band were regarded as the satellite source for the retrieval of FFL.

III. Methods

Estimating FFL included three steps, as shown in Fig. 2. First, SAIL, GeoSail, and PROSPECT RTMs were coupled to generate near-realistic forest canopy reflectance. Second, a backward inversion was undertaken, including three machine learning methods (RF, SVM, and MLP) and a traditional LUT. The third step evaluated the application value of FFL estimates concerning wildfire occurrence over the fire-prone Lushan Mountain (site 1 in Fig. 1) from 2013 through 2020. This latter step can be regarded as an alternative way to validate the performance of the coupled RTM and methods used here in addition to the quantitative validation by the FFL measurements.

A. Step1: RTMs Selection, Parameterization, and Forward Modeling

1) RTMs Selection and Coupling: To model the canopy reflectance of layered forest canopies typical in southwestern China, three RTMs (GeoSail, SAIL, and PROSPECT) were selected and coupled based on their specific application domain. For the understory, the PROSAIL RTM, which is a hybrid RTM combining the PROSPECT leaf optics model [33] and the SAIL canopy bidirectional reflectance model [30], [31], was adopted.

PROSPECT (version: PROSPECT-5) simulates leaf-level reflectance and transmittance expressed as a function of several scattering and absorption components: leaf structure parameter (N, unitless), leaf chlorophyll $a + b$ content (C_{ab}, μg/cm^2), DMC (g/cm^2), leaf equivalent water thickness (EWT, g/cm^2), leaf brown pigment (C_{bp}, unitless), and carotenoid content (C_{ar}, μg/cm^2).

The SAIL model simulates reflectance at the canopy layer as a function of a leaf inclination distribution function (LIDF), LAI (m^2/m^2), hotspot factor (hspot, unitless) [62], the sun zenith angle (tts, °), observer zenith angle (tto, °), relative azimuth angle (psi, °), leaf hemispheric reflectance (μ, simulated by the PROSPECT RTM), and leaf transmittance (τ, simulated by the PROSPECT RTM).

The PROSAILH script[3] used in this study incorporates a spectral library of background soil surfaces and uses a parameter, psoil (unitless), to characterize the effect of moisture and roughness condition on soil brightness [63], where psoil = 0 represents wet soil and psoil = 1 represents dry soil. For the LIDF, six types—including Planophile, Erectophile, Plagiophile, Extremophile, Spherical, and Uniform—were integrated into the original model script. This script also offers an alternative way to characterize the LIDF using the average leaf angle from 0° (Planophile) to 90° (Erectophile).

For the overstory, the PROSPECT RTM, coupled with the GeoSail RTM, was used to model the reflectance of the overstory (PROGeoSail RTM) since this RTM provides an approximately realistic description of the canopy reflectance of heterogeneous and discontinuous vegetation types with low computational cost [32]. The GeoSail RTM requires the parameterization of eight inputs: LIDF (unitless), leaf-level spectral reflectance (μ), and transmittance (τ) that can be modeled by the PROSPECT RTM, LAI (m^2/m^2), the spectral reflectance of the background, solar zenith angle (tts, °), the shape of the crowns (either cylinder or cone), height to width ratio of the crown (CHW, unitless), and crown coverage (ccov_1, unitless).

For modeling the overall canopy reflectance (both understory and overstory layers), the PROSAIL RTM was further coupled into PROGeoSail RTM. Total scene reflectance (ρ_t) is weighted by [32]

$$\rho_t = C\rho_c + S\rho_s + B\rho_b \tag{1}$$

where $\rho_c,\ \rho_s,\ \mathrm{and} \rho_b$ are the canopy, shadow, and background reflectance, respectively, in a specific waveband; *S* is the fraction of shadowed background; *C* is the fraction covered by the solids; and *B* is the fraction of the area that is illuminated background and can be calculated by

$$B = 1 - S - C. \tag{2}$$

The background reflectance in the shadow reflectance (ρ_s) and the illuminated background reflectance (ρ_b) were replaced by the canopy reflectance of the understory modeled by the PROSAIL RTM. For the coupled RTM, we assumed that the diffuse radiation was set as the dominant radiation for the understory layer, assuming that most of the direct radiation was intercepted by tree canopies. Therefore, the bihemispherical reflectance, rather than the bidirectional reflectance factor, of the understory was modeled in this case. Another reason for this treatment is the spectral reflectance of the background in the GeoSail RTM that is assumed to be Lambertian reflectance, while the reflectance modeled by the PROSAIL is non-Lambertian. To determine the importance of each parameter of this coupled RTM, a sensitivity analysis of this coupled RTM is given in Figs. S1 and S2 in *Supplementary Material.*

[3][Online]. Available: http://teledetection.ipgp.jussieu.fr/prosail/

TABLE I
INPUT PARAMETERS FOR THE COUPLED RTM

Parameters	Units	Symbol	Understory	Overstory
Sun zenith angle	(°)	tts_1		27–51
Leaf area index for single tree	m^2/m^2	LAI_1		0 – 5
Leaf inclination distribution function (LIDF) type		LIDF_1		Plagiophile Erectophile Spherical
Height to width ratio of the crown		CHW		1-3
Crown coverage		ccov_1		0.2-1.0
Shape of the crowns				Cone
Sun zenith angle	(°)	tts_2	30	
View zenith angle	(°)	tto	5	
Relative azimuth angle	(°)	psi	10	
Leaf area index	m^2/m^2	LAI_2	0, 1 and 2	
Hot spot factor	/	hspot	0.01	
Soil factor	/	psoil	0.5	
Leaf inclination distribution function or average leaf angle	/	LIDF_2	Spherical	
Leaf structure parameter	/	$\mathrm{N}_{1\&2}$	2	1.05-2.74 (1.54, 0.27)
Chlorophyll $a+b$ content	µg/cm^2	$\mathrm{C}_{\mathrm{ab}1\&2}$	40	0 -106.72 (41.13, 20.63)
Leaf equivalent water thickness	g/cm^2	$\mathrm{EWT}_{1\&2}$	0.005, 0.01 and 0.02	0.0001-0.029 (0.0098, 0.0037)
Dry matter content	g/cm^2	$\mathrm{DMC}_{1\&2}$	0.008	0.0018-0.0189 (0.0052, 0.0027)
Brown pigment	/	$\mathrm{C}_{\mathrm{bp}1\&2}$	0.2 – 1.5	0.2 – 1.5
Carotenoid content	µg/cm^2	$\mathrm{C}_{\mathrm{ar}1\&2}$	8	8

Here, subscript "1" denotes the overstory tree layer and "2" denotes the understory layer. The mean and standard deviation values for *N*, CAB, EWT, and DMC were given in the brackets.

2) RTMs Parameterization: To avoid the unrealistic simulations that may aggravate the ill-posed inversion problem, prior information obtained from the existing literature, leaf optical properties databases of LOPEX1993 [64] and ANGERS2003 [33], and the field measurements in southwest China were introduced to parameterize the coupled RTM. Only sensitive parameters in the coupled RTM were parameterized, whereas weak or insensitive parameters were set as fixed values, as they only exhibited a slight or no effect on the RTM outputs at the Landsat 7 ETM+ and 8 OLI bands or vegetation indices (VIs) (Figs. S1 and S2 in *Supplementary Material*). The detailed ranges and values for the coupled RTM parameterization are given in Table I. Here, the subscript "1" denotes the overstory tree layer and "2" is the understory layer.

For the understory layer, the ranges for LAI_2 (0–2) and EWT_2 (0.005–0.02) were simplified following the article presented in [38]. Other input parameters of this RTM were fixed to the model default values given that they are normally insensitive to the RTM outputs (Figs. S1 and S2 in *Supplementary Material*) and too many uncertain parameters would make the RTM inversion unstable and ill posed [39], [65]. Here, $\mathrm{LAI}_2 = 0$ indicates that the forest background is bare soil, and the coupled RTM effectively becomes the PROGeoSail RTM in such a case.

For the overstory layer, LAI_1 ranged from 0–5 based on the LAI measurements and the ancillary information extracted from

TABLE II
VIs for FFL Retrieval, Calculated From Landsat 7 ETM+ and 8 OLI Products.

VIs	Equations
Normalized Difference Vegetation Index	NDVI=(NIR – RED)/ (NIR + RED)
Enhanced Vegetation Index	EVI=2.5(NIR – RED)/ (NIR + 6RED-7.5BLUE+1)
Normalized Difference Infrared Index (band 6)	$NDII_6$=(NIR – SWIR1)/ (NIR + SWIR1)
Normalized Difference Infrared Index (band 7)	$NDII_7$=(NIR – SWIR2)/ (NIR + SWIR2)
Visible Atmospheric Resistant Index	VARI=(GREEN – RED)/ (GREEN + RED – BLUE)
Global Environmental Monitoring Index	GEMI=[μ(1 – 0.25μ) – (NIR – 0.125)]/ (1 – GREEN), μ=[2(RED^2 – NIR^2)+1.5RED+0.5NIR]/ (RED + NIR + 0.5)
Global Vegetation Moisture Index	GVMI=[(NIR + 0.1) – (SWIR1 + 0.02)]/ [(NIR + 0.1) + (SWIR1 + 0.02)]
Moisture Stress Index	MSI=SWIR1/ NIR
Greenness index	G_{ratio}= GREEN/ RED

Blue, green, red, NIR, SWIR1, and SWIR2 correspond to the blue, green, red, near-infrared, SWIR (Swir1: Band6 and Swir2: Band7 in Landsat product) bands, respectively.

the MCD15A3H MODIS LAI 06 product [66] over the field sites. $LIDF_1$ for the overstory was set as Plagiophile, Erectophile, and Spherical [67]. CHW and $ccov_1$ were parameterized to a range of 1–3 and 0.2–1, respectively, and a cone shape was used to characterize the crown shapes based on the field observations [38], [67].

At the leaf scale, N_1, C_{ab1}, EWT_1, DMC_1, C_{bp1}, and C_{ar1} in the PROSPECT-5 model for the overstory layer were parameterized by following the measurements from the leaf optical properties databases of LOPEX1993 [64] and ANGERS2003 [33]. Notably, the FFL not only includes live fuel but also dead fuel components. Therefore, the minimum values for $C_{\mathrm{ab1\&2}}$ were set to 0 and 0.0001 for the EWT, and a maximum value of 1.5 for $C_{\mathrm{bp1\&2}}$ was given for the case of dead fuel [68].

Furthermore, a Gaussian distribution was assumed for *N*, C_{ab}, EWT, and DMC for the overstory layer following their probability distribution included in the leaf optical properties databases of LOPEX1993 and ANGERS2003, whereas the rest free variables were set as uniform distribution due to the lack of enough information characterizing their probability distribution. As a result, modeled FFL can be derived as the product of LAI_1, ccov_1, and DMC_1 from the overstory layer as

$$\mathrm{FFL} = \mathrm{LAI}_1 \times \mathrm{ccov}_1 \times \mathrm{DMC}_1. \quad (3)$$

3) Ecological Information Enhanced RTM Forward Modeling: To further alleviate the ill-posed inversion, RTM simulations were constrained and regularized using ecological information. This recognizes that the input parameters of coupled RTMs are not independent of each other but naturally correlated [69]. Introducing ecological information into RTM simulations can promote more realistic scenarios given; it can decrease the probability of generating unrealistic reflectance. The ecological information for the overstory layer was predominantly extracted from the LOPEX1993 and ANGERS2003 databases. These databases represent a large range of vegetation species and, thereby, were assumed to be adequately representative. Ecological information is described in Section S2 in *Supplementary Material* and was introduced into the modeling phase through the joint posterior probability distribution of the variable correlations (i.e., the correlations between the free parameters in Table I and in *Section S2 in Supplementary Material*). This approach removed unrealistic simulation scenarios between the RTM inputs and output VIs (see Table II). The R2017a version of MATLAB.[4]

B. Step 2: RTM Backward Inversion

1) VI Selection: Nine VIs (see Table II), including the normalized difference vegetation index (NDVI) [70], enhanced vegetation index (EVI) [71], global environmental monitoring index (GEMI) [72], two normalized difference infrared indices (NDII_6 and NDII_7) [73], global vegetation moisture index (GVMI) [74], moisture stress index (MSI) [75], visible atmospheric resistant index (VARI) [76], and greenness index (G_{ratio}) [77], were selected as the potential reflectance source for FFL estimation. Of these VIs, NDVI, EVI, and GEMI are sensitive to vegetation coverage and are often used to estimate vegetation biophysical variables, including LAI [78]. NDII_6, NDII_7, GVMI, and MSI are directly related to vegetation moisture as they contain shortwave infrared (SWIR) bands and, therefore, were found to be good indicators of vegetation moisture estimates, such as fuel moisture content (FMC) [34] and CWC [79]. The VARI does not contain the SWIR band, but it has proven to be a good indicator of FMC mainly because of its sensitivity to leaf pigment variation [80]. The G_{ratio} comprises the green and red bands that are sensitive to vegetation pigment and is, therefore, commonly used for chlorophyll content estimate [77], [81]. The coefficient of determination (R^2, 5) between these VIs and the FFL measurements were evaluated separately. Only VIs with a statically significant ($p < 0.05$) association with the FFL (or LAI_1, ccov_1, and DMC_1, Figs. S1 and S2 in *Supplementary Material*) variation were selected as the optimal VIs for FFL retrieval in the next step.

2) Machine Learning Methods: Three machine learning methods (RF, SVM, and MLP) were adopted to set up the relationship between the FFL and the optimal VIs, which was achieved by training these methods using the modeled FFL (3) and the optimal VIs as input. With these trained methods, FFL was then separately estimated from the Landsat 7 ETM+ and 8 OLI data. The description and training procedure for each method is described as follows.

RF is a kind of ensemble algorithm, which belongs to the bagging (bootstrap aggregating) type. By combining multiple

[4]The Mathworks; Natick, MA, USA; (www.mathworks.com) was applied in this procedure.

weak classifiers, the final result is voted or averaged, rendering the results of the overall model to be of the highest possible accuracy and with the highly generalized performance [82], [83]. In this study, the parameters of the RF model need to be tuned to achieve optimal results. These parameters include the "number of decision trees" (tree_nums) and the "max depth of decision tree" (tree_depth). By using grid search and cross validation, all combinations of 20 tree_nums layers (10 to 200) and 10 tree_depth layers (1 to 10) were used to tune the model. Finally, the optimal parameter combinations were the case when tree_nums = 120 and tree_depth = 6.

SVM is a binary classification model and its basic core is based on the linear classification with the largest interval defined in the feature space [84]–[86]. The parameters, such as kernel function, the highest degree of a polynomial, gamma value, and penalty coefficient, need to be adjusted beforehand. Similarly, by using grid search and cross validation, the final parameters of the model were determined as kernel function = Gaussian kernel function, the highest degree of a polynomial = 3, gamma value = 1/number of features, and penalty coefficient = 1.0.

MLP is a kind of artificial neural network (ANN). Compared with the traditional ANNs, MLP has multiple hidden layers in addition to the input–output layers. The layers of the MLP are fully connected with the bottom layer as the input, the hidden middle layer, and the last layer as the output [87]. The parameters in MLP also need to be tuned. The most important parameters in MLP are the number of hidden layer's neurons, activation function, the type of weight optimizer, batch size, and learning rate. Using a similar method to that for tuning RF and SVM parameters, the best parameters for MLP were when the number of hidden layer's neurons = 100, activation function = "relu," the type of weight optimize = "the optimizer of the chance stochastic gradient," batch size = 200, and learning rate = 0.001.

3) LUT Inversion: The performance of the three machine learning methods was compared with a commonly used LUT inversion method. An LUT was built by running the parameterized coupled RTM forward, recording the relationship between free variables (i.e., tts_1, LAI_1, CHW, ccov_1, LAI_2, N_1, $C_{\mathrm{ab}1}$ $\mathrm{EWT}_{1\&2}$, DMC_1, and $C_{\mathrm{bp}1\&2}$ in Table I) and the corresponding VIs. The objective of this method is to find which of the simulated reflectances stored in the LUT are closer to each of the observed VIs through a cost function (4) as

$$J(v, w) = \sqrt{\frac{\sum_{i=1}^{n} (v_i - w_i)^2}{n}} \tag{4}$$

where n is the number of observations, v denotes the observed VIs from Landsat ETM+ and 8 OLI data, and w denotes the modeled VIs in the LUT. Normally, the optimal solution searched by a cost function was not always unique due to the ill-posed inverse problem [49]. Following previous studies [34], [88], the mean value of the 40 best-fitted solutions [i.e., the $f(v,w)$ values or the modeled FFL in (3)] was recorded as the final retrieved FFL to make the retrieved FFL consistent.

4) Validation: The accuracy levels of retrieved FFL derived from the four inversion methods were evaluated using the data from sites in southwest China and Sweden with the assumption

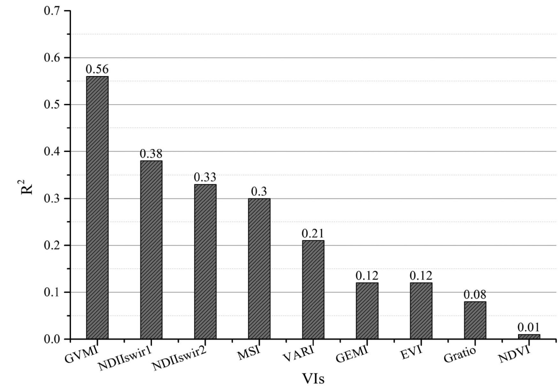

Fig. 3. R^2 values associated with FFL measurements and Landsat 8 OLI and 7 ETM+ derived nine VIs.

that these methods were feasible for application in different regions, species, and circumstances. Three metrics were adopted to characterize the accuracy level of FFL estimates, being R^2 (5), root-mean-square deviation (RMSE, 6), and relative RMSE (rRMSE, 7).

$$R^2 = 1 - \frac{\sum_{i=1}^{m} (M_i - E_i)^2}{\sum_{i=1}^{m} (M_i - \overline{M}_i)^2} \tag{5}$$

$$\mathrm{RMSE} = \sqrt{\frac{\sum_{i=1}^{m} (M_i - E_i)^2}{m}} \tag{6}$$

$$\mathrm{rRMSE} = \frac{\mathrm{RMSE}}{\overline{M_i}} \tag{7}$$

where M_i and E_i are the ith measured and estimated FFL, $\overline{M_i}$ is the mean value of FFL measurements, and m is the number of observations. The rRMSE is calculated as RMSE divided by the mean of the variable measured in the field, which allows comparison between the variables of different ranges since it is insensitive to the magnitude of values and less sensitive to outliers [63].

C. Step 3: Evaluation of Applicability

The FFL dynamics for the Lushan Mountain area (Site 1 in Fig. 1) from 2013 through 2020 were mapped under the high-performance parallel and stream computing framework using the best inversion method (i.e., RTM + MLP) and the Landsat 8 OLI data. Here, only images with the cloud coverage of less than 10% were used for the mapping, whereas the remaining images were excluded. The applicable value of the FFL dataset was then evaluated by analyzing the relationship between the sum of 16-day interval FFL ($\mathrm{FFL}_{\mathrm{sum}}$) and these two wildfire events in 2014 and 2020 (see Fig. 1).

IV. Results

A. Evaluation of the Four RTM Inversion Methods

The R^2 values associated with FFL measurements and the selected nine VIs are illustrated in Fig. 3, among which the GVMI outperformed the other VIs (R^2 = 0.56), followed by

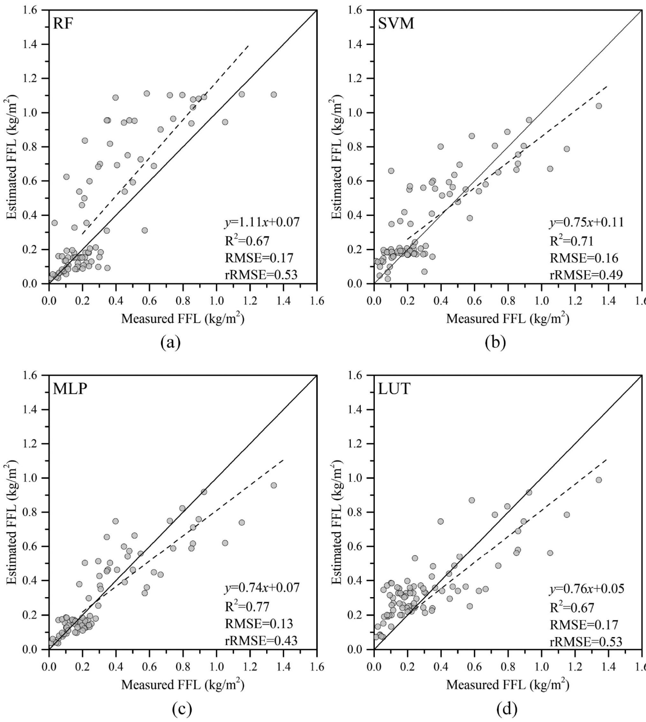

Fig. 4. Estimated versus measured FFL using (a) RF, (b) SVM, (c) MLP, and (d) LUT methods.

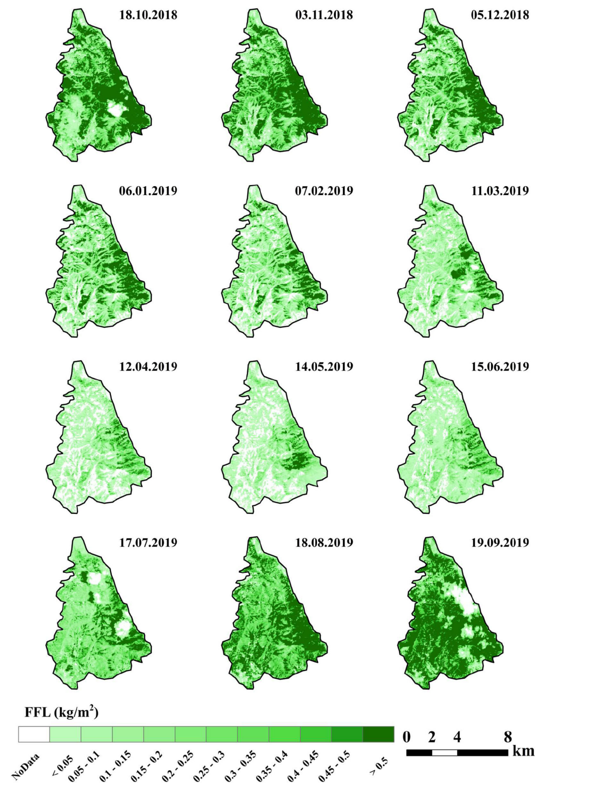

Fig. 5. FFL mapping for the Lushan Mountain area from 2018 through 2019 from Landsat 8 OLI product.

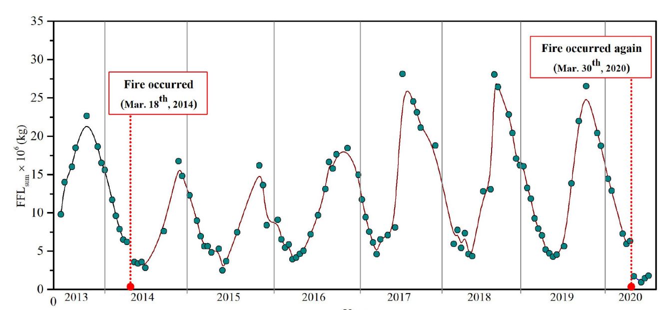

Fig. 6. Sum of 16-day interval FFL ($\mathrm{FFL}_{\mathrm{sum}}$, green points) dynamics for Lushan Mountain forest from 2013 through 2020 based on Landsat 8 OLI data. These points were fitted with a B-Spline curve using OriginPro software (version: 9.0). Two forest fires occurred during this period, as shown in Fig. 1, causing a clear decrease in $\mathrm{FFL}_{\mathrm{sum}}$.

NDII_6, NDII_7, MSI, and VARI that demonstrated reasonable performance ($R^2 > 0.2$). Associations between FFL measurements and GEMI, EVI, G_{ratio}, and NDVI were poor, exhibiting a low correlation ($R^2 < 0.2$). Therefore, combined with the total sensitivity index value from Fig. S2 in *Supplementary Material*, GVMI, NDII_6, NDII_7, MSI, and VARI were determined as the optimal VI combination for FFL retrieval.

By linking the RTM simulation with the three machine learning methods and the LUT, FFL was estimated from the Landsat 7 ETM+ (for Sweden) and 8 OLI data (for southwest China) (see Fig. 4). In general, the SVM (Fig. 4(b), $R^2 = 0.71$, RMSE = 0.16, and rRMSE = 0.49) and MLP (Fig. 4(c), $R^2 = 0.77$, RMSE = 0.13, and rRMSE = 0.43) outperformed the LUT (Fig. 4(d), $R^2 = 0.67$, RMSE = 0.17, and rRMSE = 0.53) with higher R^2 values and lower RMSE and rRMSE values, whereas a similar accuracy level was found for both RF and LUT (Fig. 4(a), $R^2 = 0.67$, RMSE = 0.17, and rRMSE = 0.53). The MLP method showed the highest accuracy level among these three methods. However, the high values were generally underestimated (or saturated) when the FFL > 0.9 kg/m^2, which can also be detected in the SVM and LUT cases. Conversely, most high values for the RF were overestimated. For the low FFL range (<0.4 kg/m^2), all the machine learning methods outperformed the LUT that generally overestimated FFL.

B. FFL Mapping and Dynamics in Response to Wildfire Occurrence

FFL maps generated for the Lushan Mountain forest using the trained MLP method and Landsat 8 OLI product are presented in Fig. 5. FFL is normally high from August through December and then gradually declines with the onset of the typical fire season that lasts from January to June. During this period, the live foliage of deciduous forest in the western area gradually cures into dead foliage and is shed from branches, whereas less variation was observed for the evergreen forest located in the eastern area. With the beginning of the rainy season starting in July, the FFL increases rapidly.

Fig. 6 shows the annual $\mathrm{FFL}_{\mathrm{sum}}$ dynamics (i.e., the B-Spline curved fitted by OriginPro software, version: 9.0) in the Lushan mountainous area, which is mapped from the RTM combined with MLP method and Landsat 8 OLI data from 2013 through 2020 (Step 3 in Section III). A clear decrease of the $\mathrm{FFL}_{\mathrm{sum}}$ can be observed after the wildfire on the 18th of March, 2014, after which the $\mathrm{FFL}_{\mathrm{sum}}$ recovered but was still in a low condition until 2017. After 2017, FFL reached a critical point (around 27

$\times 10^6$ kg). Effectively, the last fire in 2014 burned most of the FFL but the $\mathrm{FFL_{sum}}$ accumulated for 3 to 6 years and reached a higher peak. Under this condition, the forest burned again on the 30th March, 2020, causing a greater decrease of the $\mathrm{FFL_{sum}}$ than was the case for the previous fire.

V. Discussion

This study applied Landsat 7 ETM+ and 8 OLI data for FFL monitoring by linking a coupled RTM with machine learning methods. The FFL dynamics at Lushan Mountain from 2013 through 2020 showed that this satellite-derived FFL dataset can be used to provide insights into FFL dynamics. It is anticipated that the methods for estimating FFL can be applied for crown fire potential and firefighter safety assessment in the future.

The FFL estimates from the four methods were within a reasonable range (R^2: 0.67–0.77, RMSE: 0.13–0.17, and rRMSE: 0.43–0.53) and exhibited statistically significant ($p < 0.01$) agreement between the estimates and observations. However, FFL estimates generated from SVM, MLP, and LUT became saturated when FFL was greater than 0.9 kg/m^2, whereas the RF approach overestimated FFL. This may be a drawback of the optical remote sensing data, given that the optical band cannot penetrate the densely covered forest. For the RF case, the overestimation problem may be caused by its higher sensitivity to the "noise" related to the coupled RTM—such as the scenario of forest trees being assumed to be an ideal cone or cylinder, the parameterization of the RTM, or the uncertainty of the prior information incorporated—than the case for the SVM and MLP approaches. If the training data are large enough with lower noise, the performance of RF should be improved [89], [90]. On the other hand, the high performance of the MLP and SVM indicated that these methods can handle this "noise" in the dataset and, therefore, can generate stable FFL estimates.

Rather than the use of band reflectance, nine VIs were selected as the reflectance sources to retrieve the FFL due to their capacity to minimize the topographic effects on the reflected radiance [91] and high sensitivity to vegetation properties. Instead of using all of the VIs, a combination of GVMI, $\mathrm{NDII_6}$, $\mathrm{NDII_7}$, MSI, and VARI was used. Interestingly, these VIs were sensitive to vegetation moisture properties as they contain the SWIR band, except VARI that was also demonstrated by a previous study to be a good indicator for vegetation moisture property estimates [80]. These VIs are also sensitive to DMC [35] (an important element for FFL estimate) dynamic, but the EWT is usually greater than DMC, resulting in the retrieval of DMC from RTM being challenging [92]. Nevertheless, a high correlation between EWT and DMC was found for these forest species (see Fig. 3), which enhanced the sensitivity of these vegetation moisture-related VIs to DMC. This may be one of the reasons explaining the usefulness of these VIs in deriving the FFL. Conversely, it was surprising that NDVI and EVI, particularly NDVI, showed a low correlation with FFL since these VIs have been proven to be sensitive to the vegetation coverage (or LAI). One possible explanation is that NDVI can be easily saturated with the increase of LAI, and therefore, it is not suitable for deriving the properties of dense forest, particularly for the forest in Sweden.

For the quantitative estimation of vegetation variables from the satellite data, the debate about the traditional statistical methods versus physical model (including RTMs) inversion has been longstanding. Regarding fuel load estimation from remote sensing data, previous studies usually adopted statistical methods due to the ease of use and reasonable accuracy level [22], [23], [24], [93], whereas in this study, the RTM inversion was undertaken. We argue that the RTM inversion method has the unique advantage of providing a clear explanation of why FFL can be estimated from remote sensing data, in a physical sense, while this is less clear using statistical methods. For most RTMs, two critical variables are included to describe the properties of canopy and leaf at the pixel scale, being average LAI (m^2/m^2) and DMC (g/m^2). Based on the definition of these variables, we argue that FFL can essentially be derived. Moreover, the RTM can not only be used to simulate the reflectance of live fuel but also the dead fuel by adjusting the range and values of the model input parameters (Section III-A2). Because of this clear relationship between the FFL and the canopy reflectance, the RTM inversion method can be applied in other areas if the model is well parameterized. However, the RTM inversion method presented in the study also has the drawbacks that it cannot model and retrieve the fuel load of fine branches (<6 mm), which is also an important indicator for crown fire danger. Microwave data can be useful for fine branch fuel load estimation as it has a longer waveband than the optical waveband [22].

We argue that the coupled RTM can more realistically describe the reflectance of the two-layered forest in southwest China. However, this coupling requires more input parameters, which may aggravate the ill-posed inversion problem if the RTM contains too many parameters [39]], [65], thus making the inversion unstable. For this reason, only a limited set of values were used to parameterize the PROSAIL RTM for the understory layer with most of its parameters being fixed, based on field surveys and a sensitivity analysis of the coupled RTM (Figs. S1 and S2 in *Supplementary Material*). Reasonable FFL estimates demonstrated the feasibility of this RTM coupling and proved its reproducibility value to be applied in Sweden where the forest characters were unknown.

The FFL for both needle leaf and broadleaf trees was estimated in this study using the same PROSPECT RTM. Theoretically, the PROSPECT RTM was designed for simulating the reflectance and transmittance of the broadleaf forest. For needle leaf forest, the LIBERTY RTM [94] should theoretically be more appropriate. However, given that previous studies demonstrated that the PROSPECT RTM also performed well for retrieving vegetation variables of needle leaf forest [95]–[97], and given that it is simpler than the LIBERTY RTM with fewer input parameters, the PROSPECT RTM was used here. Additionally, the reasonable accuracy of the FFL estimates also demonstrated the feasibility of the PROSPECT RTM for needle FFL estimation.

VI. Conclusion

This study monitored and retrieved forest FFL by linking RTMs with three machine learning methods from Landsat 7 ETM+ and 8 OLI products. The GeoSail, SAIL, and PROSPECT RTMs were coupled and carefully parameterized from available information. Three machine learning methods (RF, SVM, and MLP) were applied to link the coupled RTM with its simulations and then derive FFL estimates from the satellite observations. The performances of these methods were also compared with the traditional LUT method. Quantitative validations using the measurements from southwest China and Sweden showed that these machine learning methods performed with similar (RF) or better (SVM and MLP) accuracy than the LUT method, whereas the MLP outperformed the other two machine learning methods. The FFL dynamics in the Lushan mountain from 2013 through 2020 showed that this satellite-derived FFL dataset can be used to serve the local fire managers for estimating FFL with the anticipation that it can also assist in wildfire danger early prediction, suppression, and response for this region.

Acknowledgment

The authors would like to thank the ONERA, ESA, and BioSAR team for providing the BioSAR 2008 datasets for validating the performance of the methodology presented in this study.

References

[1] A. Massetti, C. Rudiger, M. Yebra, and J. Hilton, “The vegetation structure perpendicular index (VSPI): A forest condition index for wildfire predictions,” *Remote Sens. Environ.,* vol. 224, pp. 167–181, 2019.

[2] R. E. Keane, R. E. Burgan, and J. W. van Wagtendonk, “Mapping wildland fuels for fire management across multiple scales: Integrating remote sensing, GIS, and biophysical modeling,” *Int. J. Wildland Fire,* vol. 10, no. 4, pp. 301–319, 2001.

[3] E. Chuvieco, *Wildland Fire Danger: Estimation and Mapping: The Role of Remote Sensing Data*. Singapore: World Scientific, 2003.

[4] R. M. Reich, J. E. Lundquist, and V. A. Bravo, “Spatial models for estimating fuel loads in the Black Hills, South Dakota, USA,” *Int. J. Wildland Fire,* vol. 13, no. 1, pp. 119–129, 2004.

[5] J. S. Gould, W. L. McCaw, and N. P. Cheney, “Quantifying fine fuel dynamics and structure in dry Eucalypt forest *(Eucalyptus marginata)* in Western Australia for fire management,” *Forest Ecol. Manage.,* vol. 262, no. 3, pp. 531–546, 2011.

[6] J. H. Scott and E. D. Reinhardt, *Assessing Crown Fire Potential by Linking Models of Surface and Crown Fire Behavior*. Fort Collins, CO, USA: US Dept. Agriculture Forest Service, Rocky Mountain Research Station, 2001.

[7] K. Brandis and C. Jacobson, “Estimation of vegetative fuel loads using Landsat TM imagery in New South Wales, Australia,” *Int. J. Wildland Fire,* vol. 12, no. 2, pp. 185–194, 2003.

[8] I. D. Mitsopoulos and A. P. Dimitrakopoulos, “Allometric equations for crown fuel biomass of Aleppo pine *(Pinus halepensis mill.)* in Greece,” *Int. J. Wildland Fire,* vol. 16, no. 5, pp. 642–647, 2007.

[9] C. E. van Wagner, “Conditions for the start and spread of crown fire,” *Can. J. Forest Res.,* vol. 7, no. 1, pp. 23–34, 1977.

[10] K. L. Gray and E. Reinhardt, “Analysis of algorithms for predicting canopy fuel,” in *Proc. 2nd Int. Wildland Fire Ecol. Fire Manage. Congr. 5th Symp. Fire Forest Meteorol.* 2003, pp. 5–8.

[11] G. Mallinis, I. Mitsopoulos, P. Stournara, P. Patias, and A. Dimitrakopoulos, “Canopy fuel load mapping of mediterranean pine sites based on individual tree-crown delineation,” *Remote Sens.,* vol. 5, no. 12, pp. 6461–6480, 2013.

[12] W.-P. Zhang, X. Jia, E. C. Morris, Y.-Y. Bai, and G.-X. Wang, “Stem, branch and leaf biomass-density relationships in forest communities,” *Ecol. Res.,* vol. 27, no. 4, pp. 819–825, 2012.

[13] O. Kucuk, B. Saglam, and E. Bilgili, “Canopy fuel characteristics and fuel load in young black pine trees,” *Biotechnol. Biotechnol. Equip.*, vol. 21, no. 2, pp. 235–240, 2014.

[14] Ö. Küçük, E. Bilgili, and B. Sağlam, “Estimating crown fuel loading for Calabrian pine and Anatolian black pine,” *Int. J. Wildland Fire*, vol. 17, no. 1, pp. 147–154, 2008.

[15] J. H. Kotecha and P. M. Djuric, “Gaussian sum particle filtering,” *IEEE Trans. Signal Process.,* vol. 51, no. 10, pp. 2602–2612, Oct. 2003.

[16] S. Jin and S.-C. Chen, “Application of QuickBird imagery in fuel load estimation in the Daxinganling region, China,” *Int. J. Wildland Fire,* vol. 21, no. 5, pp. 583–590, 2012.

[17] Z. Li *et al.*, “Assessment of fire fuel load dynamics in shrubland ecosystems in the western United States using MODIS products,” *Remote Sens.*, vol. 12, no. 12, 2020.

[18] P. J. Zarco-Tejada, A. Hornero, P. S. A. Beck, T. Kattenborn, P. Kempeneers, and R. Hernandez-Clemente, “Chlorophyll content estimation in an open-canopy conifer forest with Sentinel-2A and hyperspectral imagery in the context of forest decline,” *Remote Sens. Environ.*, vol. 223, pp. 320–335, Mar. 15, 2019.

[19] J. He, T. V. Loboda, L. Jenkins, and D. Chen, “Mapping fractional cover of major fuel type components across Alaskan tundra,” *Remote Sens. Environ.*, vol. 232, 2019, Art. no. 111324.

[20] M. García, D. Riano, E. Chuvieco, J. Salas, and F. M. Danson, “Multispectral and LiDAR data fusion for fuel type mapping using support vector machine and decision rules,” *Remote Sens. Environ.,* vol. 115, no. 6, pp. 1369–1379, 2011.

[21] A. Alonso-Benito, L. Arroyo, M. Arbelo, and P. Hernandez Leal, “Fusion of Worldview-2 and LiDAR data to map fuel types in the Canary islands,” *Remote Sens.,* vol. 8, no. 8, 2016, Art. no. 669.

[22] S. Saatchi, K. Halligan, D. G. Despain, and R. L. Crabtree, “Estimation of forest fuel load from radar remote sensing,” *IEEE Trans. Geosci. Remote Sens.*, vol. 45, no. 6, pp. 1726–1740, Jun. 2007.

[23] J. Franke *et al.*, “Fuel load mapping in the Brazilian Cerrado in support of integrated fire management,” *Remote Sens. Environ.,* vol. 217, pp. 221–232, 2018.

[24] N. Skowronski, K. Clark, R. Nelson, J. Hom, and M. Patterson, “Remotely sensed measurements of forest structure and fuel loads in the Pinelands of New Jersey,” *Remote Sens. Environ.,* vol. 108, no. 2, pp. 123–129, 2007.

[25] X. Zhang and S. Kondragunta, “Estimating forest biomass in the USA using generalized allometric models and MODIS land products,” *Geophys. Res. Lett.,* vol. 33, no. 9, May 11, 2006.

[26] L. Wang, E. Hunt, J. Qu, X. Hao, and C. S. T. Daughtry, “Towards estimation of canopy foliar biomass with spectral reflectance measurements,” *Remote Sens. Environ.,* vol. 115, no. 3, pp. 836–840, Mar. 15, 2011.

[27] X. Quan *et al.*, “A radiative transfer model-based method for the estimation of grassland aboveground biomass,” *Int. J. Appl. Earth Observ. Geoinf.,* vol. 54, pp. 159–168, Feb. 2017.

[28] M. G. Gale, G. J. Cary, A. I. J. M. van Dijk, and M. Yebra, “Forest fire fuel through the lens of remote sensing: Review of approaches, challenges and future directions in the remote sensing of biotic determinants of fire behaviour,” *Remote Sens. Environ.,* vol. 255, 2021, Art. no. 112282.

[29] M. Yebra *et al.*, “A global review of remote sensing of live fuel moisture content for fire danger assessment: Moving towards operational products,” *Remote Sens. Environ.,* vol. 136, pp. 455–468, Sep. 2013.

[30] W. Verhoef, “Theory of radiative transfer models applied in optical remote sensing of vegetation canopies,” Ph.D. dissertation, Dep. Nat. Aerosp. Lab., Amsterdam, The Netherlands, 1998.

[31] W. Verhoef, “Light scattering by leaf layers with application to canopy reflectance modeling: The SAIL model,” *Remote Sens. Environ.,* vol. 16, no. 2, pp. 125–141, Oct. 1984.

[32] K. F. Huemmrich, “The geosail model: A simple addition to the SAIL model to describe discontinuous canopy reflectance,” *Remote Sens. Environ.,* vol. 75, no. 3, pp. 423–431, Mar. 2001.

[33] J. B. Feret *et al.*, “PROSPECT-4 and 5: Advances in the leaf optical properties model separating photosynthetic pigments,” *Remote Sens. Environ.,* vol. 112, no. 6, pp. 3030–3043, Jun. 16, 2008.

[34] M. Yebra, X. Quan, D. Riaño, P. R. Larraondo, A. I. J. M. van Dijk, and G. J. Cary, “A fuel moisture content and flammability monitoring methodology for continental Australia based on optical remote sensing,” *Remote Sens. Environ.,* vol. 212, pp. 260–272, 2018.

[35] P. Bowyer and F. M. Danson, “Sensitivity of spectral reflectance to variation in live fuel moisture content at leaf and canopy level,” *Remote Sens. Environ.,* vol. 92, no. 3, pp. 297–308, Aug. 30, 2004.

[36] P. Bicheron and M. Leroy, “A method of biophysical parameter retrieval at global scale by inversion of a vegetation reflectance model,” *Remote Sens. Environ.,* vol. 67, no. 3, pp. 251–266, Mar. 1999.

[37] B. Combal *et al.*, “Retrieval of canopy biophysical variables from bidirectional reflectance: Using prior information to solve the ill-posed inverse problem,” *Remote Sens. Environ.,* vol. 84, no. 1, pp. 1–15, 2003.

[38] X. Quan, B. He, M. Yebra, C. Yin, Z. Liao, and X. Li, “Retrieval of forest fuel moisture content using a coupled radiative transfer model,” *Environ. Model. Softw.,* vol. 95, pp. 290–302, Sep. 2017.

[39] M. Yebra and E. Chuvieco, "Generation of a species-specific look-up table for fuel moisture content assessment," *IEEE J. Sel. Topics Appl. Earth Observ. Remote Sens.,* vol. 2, no. 1, pp. 21–26, Mar. 2009.

[40] M. Yebra, E. Chuvieco, and D. Riano, "Estimation of live fuel moisture content from MODIS images for fire risk assessment," *Agricultural Forest Meteorol.,* vol. 148, no. 4, pp. 523–536, Apr. 16, 2008.

[41] M. Schlerf and C. Atzberger, "Inversion of a forest reflectance model to estimate structural canopy variables from hyperspectral remote sensing data," *Remote Sens. Environ.,* vol. 100, no. 3, pp. 281–294, Feb. 15, 2006.

[42] H. Fang, S. Liang, and A. Kuusk, "Retrieving leaf area index using a genetic algorithm with a canopy radiative transfer model," *Remote Sens. Environ.,* vol. 85, no. 3, pp. 257–270, 2003.

[43] M. Trombetti, D. Riaño, M. A. Rubio, Y. B. Cheng, and S. L. Ustin, "Multi-temporal vegetation canopy water content retrieval and interpretation using artificial neural networks for the continental USA," *Remote Sens. Environ.,* vol. 112, no. 1, pp. 203–215, Jan. 15, 2008.

[44] J. Qin, S. Liang, X. Li, and J. Wang, "Development of the adjoint model of a canopy radiative transfer model for sensitivity study and inversion of leaf area index," *IEEE Trans. Geosci. Remote Sens.,* vol. 46, no. 7, pp. 2028–2037, Jul. 2008.

[45] J. Verrelst, J. P. Rivera, G. Leonenko, L. Alonso, and J. Moreno, "Optimizing LUT-based RTM inversion for semiautomatic mapping of crop biophysical parameters from Sentinel-2 and -3 data: Role of cost functions," *IEEE Trans. Geosci. Remote Sens.,* vol. 52, no. 1, pp. 257–269, Jan. 2014.

[46] B. Combal, F. Baret, and M. Weiss, "Improving canopy variables estimation from remote sensing data by exploiting ancillary information: Case study on sugar beet canopies," *Agronomie,* vol. 22, no. 2, pp. 205–215, Mar. 2002.

[47] R. Houborg, M. Anderson, and C. Daughtry, "Utility of an image-based canopy reflectance modeling tool for remote estimation of LAI and leaf chlorophyll content at the field scale," *Remote Sens. Environ.,* vol. 113, no. 1, pp. 259–274, Jan. 15, 2009.

[48] J. Verrelst *et al.*, "Experimental Sentinel-2 LAI estimation using parametric, non-parametric and physical retrieval methods—A comparison," *ISPRS J. Photogramm. Remote Sens.,* vol. 108, pp. 260—272, 2015.

[49] R. Darvishzadeh, A. Skidmore, M. Schlerf, and C. Atzberger, "Inversion of a radiative transfer model for estimating vegetation LAI and chlorophyll in a heterogeneous grassland," *Remote Sens. Environ.*, vol. 112, no. 5, pp. 2592–2604, May 15, 2008.

[50] L. Zhong, L. Hu, and H. Zhou, "Deep learning based multi-temporal crop classification," *Remote Sens. Environ.*, vol. 221, pp. 430–443, 2019.

[51] M. Wieland, Y. Li, and S. Martinis, "Multi-sensor cloud and cloud shadow segmentation with a convolutional neural network," *Remote Sens. Environ.*, vol. 230, 2019, Art. no. 111203.

[52] C. Xiao, N. Chen, C. Hu, K. Wang, J. Gong, and Z. Chen, "Short and mid-term sea surface temperature prediction using time-series satellite data and LSTM-AdaBoost combination approach," *Remote Sens. Environ.,* vol. 233, 2019, Art. no. 111358.

[53] G. Camps-Valls, J. Verrelst, J. Munoz-Mari, V. Laparra, F. Mateo-Jimenez, and J. Gomez-Dans, "A survey on Gaussian processes for earth-observation data analysis: A comprehensive investigation," *IEEE Geosci. Remote Sens. Mag.,* vol. 4, no. 2, pp. 58–78, Jun. 2016.

[54] U. B. Gewali, S. T. Monteiro, and E. Saber, "Gaussian processes for vegetation parameter estimation from hyperspectral data with limited ground truth," *Remote Sens.,* vol. 11, no. 13, 2019, Art. no. 1614.

[55] D. H. Svendsen, P. Morales-Álvarez, A. B. Ruescas, R. Molina, and G. Camps-Valls, "Deep Gaussian processes for biogeophysical parameter retrieval and model inversion," *ISPRS J. Photogramm. Remote Sens.,* vol. 166, pp. 68–81, 2020.

[56] D. H. Svendsen, L. Martino, M. Campos-Taberner, F. J. García-Haro, and G. Camps-Valls, "Joint Gaussian processes for biophysical parameter retrieval," *IEEE Trans. Geosci. Remote Sens.*, vol. 56, no. 3, pp. 1718–1727, Mar. 2018.

[57] A. Wolanin *et al.*, "Estimating crop primary productivity with Sentinel-2 and Landsat 8 using machine learning methods trained with radiative transfer simulations," *Remote Sens. Environ.,* vol. 225, pp. 441–457, 2019.

[58] H. Shi, Z. Xiao, and X. Tian, "Exploration of machine learning techniques in emulating a coupled soil–canopy–atmosphere radiative transfer model for multi-parameter estimation from satellite observations," *IEEE Trans. Geosci. Remote Sens.,* vol. 57, no. 11, pp. 8522–8533, Nov. 2019.

[59] I. Hajnsek *et al.*, "BIOSAR 2008: Data acquistion and processing report," 2009.

[60] N. Gorelick, M. Hancher, M. Dixon, S. Ilyushchenko, D. Thau, and R. Moore, "Google Earth Engine: Planetary-scale geospatial analysis for everyone," *Remote Sens. Environ.,* vol. 202, pp. 18–27, 2017.

[61] P. Scaramuzza and J. Barsi, "Landsat 7 scan line corrector-off gap-filled product development," in *Proc. Pecora*, 2005, pp. 23–27.

[62] A. Kuusk, *The Hot-Spot Effect in Plant Canopy Reflectance*, R. B. Myneni and J. Ross, Eds. New York, NY, USA: Springer, 1991, pp. 139–159.

[63] A. Casas, D. Riaño, S. L. Ustin, P. Dennison, and J. Salas, "Estimation of water-related biochemical and biophysical vegetation properties using multitemporal airborne hyperspectral data and its comparison to MODIS spectral response," *Remote Sens. Environ.,* vol. 148, pp. 28–41, May 25, 2014.

[64] B. Hosgood *et al.*, "Leaf optical properties experiment 93 (LOPEX93)," Eur. Commission, Joint Res. Centre, Inst. Remote Sens. Appl., Ispra, Italy, 1995.

[65] W. Verhoef and H. Bach, "Coupled soil–leaf-canopy and atmosphere radiative transfer modeling to simulate hyperspectral multi-angular surface reflectance and TOA radiance data," *Remote Sens. Environ.,* vol. 109, no. 2, pp. 166–182, 2007.

[66] R. B. Myneni *et al.*, "Global products of vegetation leaf area and fraction absorbed PAR from year one of MODIS data," *Remote Sens. Environ.,* vol. 83, no. 1/2, pp. 214–231, Nov. 2002.

[67] S. Jurdao, M. Yebra, J. P. Guerschman, and E. Chuvieco, "Regional estimation of woodland moisture content by inverting radiative transfer models," *Remote Sens. Environ.,* vol. 132, pp. 59–70, May 2013.

[68] M. Lang, T. Nilson, A. Kuusk, and A. Kiviste, "The performance of different leaf mass and crown diameter models in forming the input of a forest reflectance model: A test on forest growth sampleplots and Landsat ETM images," in *Proc. Forest Sat*, 2005, pp. 41–45.

[69] M. Yebra and E. Chuvieco, "Linking ecological information and radiative transfer models to estimate fuel moisture content in the Mediterranean region of Spain: Solving the ill-posed inverse problem," *Remote Sens. Environ.,* vol. 113, no. 11, pp. 2403–2411, Nov. 16, 2009.

[70] C. J. Tucker, "Red and photographic infrared linear combinations for monitoring vegetation," *Remote Sens. Environ.,* vol. 8, no. 2, pp. 127–150, 1979.

[71] A. Huete, K. Didan, T. Miura, E. P. Rodriguez, X. Gao, and L. G. Ferreira, "Overview of the radiometric and biophysical performance of the MODIS vegetation indices," *Remote Sens. Environ.,* vol. 83, no. 1/2, pp. 195–213, Nov. 2002.

[72] B. Pinty and M. Verstraete, "GEMI: A non-linear index to monitor global vegetation from satellites," *Vegetatio,* vol. 101, no. 1, pp. 15–20, 1992.

[73] M. Hardisky, V. Klemas, and R. M. Smart, "The influence of soil salinity, growth form, and leaf moisture on the spectral radiance of Spartina alterniflora canopies," *Photogramm. Eng. Remote Sens.,* vol. 49, pp. 77–83, 1983.

[74] P. Ceccato, N. Gobron, S. Flasse, B. Pinty, and S. Tarantola, "Designing a spectral index to estimate vegetation water content from remote sensing data: Part 1—Theoretical approach," *Remote Sens. Environ.*, vol. 82, no. 2/3, pp. 188–197, Oct. 2002.

[75] B. N. Rock, J. E. Vogelmann, D. L. Williams, A. F. Vogelmann, and T. Hoshizaki, "Remote detection of forest damage: Plant responses to stress may have spectral 'signatures' that could be used to map, monitor, and measure forest damage," *BioScience,* vol. 36, no. 7, pp. 439–445, 1986.

[76] A. A. Gitelson, R. Stark, U. Grits, D. Rundquist, Y. Kaufman, and D. Derry, "Vegetation and soil lines in visible spectral space: A concept and technique for remote estimation of vegetation fraction," *Int. J. Remote Sens.,* vol. 23, no. 13, pp. 2537–2562, Jul. 10, 2002.

[77] P. Zarcotejada *et al.*, "Assessing vineyard condition with hyperspectral indices: Leaf and canopy reflectance simulation in a row-structured discontinuous canopy," *Remote Sens. Environ.,* vol. 99, no. 3, pp. 271–287, 2005.

[78] R. Houborg, H. Soegaard, and E. Boegh, "Combining vegetation index and model inversion methods for the extraction of key vegetation biophysical parameters using terra and aqua MODIS reflectance data," *Remote Sens. Environ.,* vol. 106, no. 1, pp. 39–58, Jan. 15, 2007.

[79] F. J. García-Haro *et al.*, "A global canopy water content product from AVHRR/Metop," *ISPRS J. Photogramm. Remote Sens.,* vol. 162, pp. 77–93, 2020.

[80] G. Caccamo, L. A. Chisholm, R. A. Bradstock, M. L. Puotinen, and B. G. Pippen, "Monitoring live fuel moisture content of heathland, shrubland and sclerophyll forest in south-eastern Australia using MODIS data," *Int. J. Wildland Fire,* vol. 21, no. 3, pp. 257–269, 2012.

[81] C. Yin, B. He, X. Quan, and Z. Liao, "Chlorophyll content estimation in arid grasslands from Landsat-8 OLI data," *Int. J. Remote Sens.,* vol. 37, no. 3, pp. 615–632, Feb. 2016.

[82] M. Belgiu and L. Drăguţ, “Random forest in remote sensing: A review of applications and future directions,” *ISPRS J. Photogramm. Remote Sens.,* vol. 114, pp. 24–31, 2016.

[83] F. Guo *et al.*, “What drives forest fire in Fujian, China? Evidence from logistic regression and random forests,” *Int. J. Wildland Fire,* vol. 25, no. 5, pp. 505–519, 2016.

[84] M. Rodrigues and J. de la Riva, “An insight into machine-learning algorithms to model human-caused wildfire occurrence,” *Environ. Model. Softw.,* vol. 57, pp. 192–201, 2014.

[85] A. Widodo and B.-S. Yang, “Support vector machine in machine condition monitoring and fault diagnosis,” *Mech. Syst. Signal Process.,* vol. 21, no. 6, pp. 2560–2574, 2007.

[86] L. J. Cao and F. H. Tay, “Support vector machine with adaptive parameters in financial time series forecasting,” *IEEE Trans. Neural Netw.,* vol. 14, no. 6, pp. 1506–1518, Nov. 2003.

[87] J. Tang, C. Deng, and G. B. Huang, “Extreme learning machine for multilayer perceptron,” *IEEE Trans. Neural Netw. Learn. Syst.,* vol. 27, no. 4, pp. 809–821, Apr. 2016.

[88] M. Weiss, F. Baret, R. B. Myneni, A. Pragnère, and Y. Knyazikhin, “Investigation of a model inversion technique to estimate canopy biophysical variables from spectral and directional reflectance data,” *Agronomie,* vol. 20, no. 1, pp. 3–22, 2000.

[89] L. Breiman, J. H. Friedman, C. J. Stone, and R. A. Olshen, *Classification and Regression Trees*. Boca Raton, FL, USA: CRC Press, 1984.

[90] L. Breiman, “Random forests,” *Mach. Learn.,* vol. 45, no. 1, pp. 5–32, 2001.

[91] B. Matsushita, W. Yang, J. Chen, Y. Onda, and G. Qiu, “Sensitivity of the enhanced vegetation index (EVI) and normalized difference vegetation index (NDVI) to topographic effects: A case study in high-density Cypress forest,” *Sensors,* vol. 7, no. 11, pp. 2636–2651, Nov. 5, 2007.

[92] D. Riaño, P. Vaughan, E. Chuvieco, P. J. Zarco-Tejada, and S. L. Ustin, “Estimation of fuel moisture content by inversion of radiative transfer models to simulate equivalent water thickness and dry matter content: Analysis at leaf and canopy level,” *IEEE Trans. Geosci. Remote Sens.,* vol. 43, no. 4, pp. 819–826, Apr. 2005.

[93] F. J. Romero Ramirez, R. M. Navarro-Cerrillo, M. Á. Varo-Martínez, J. L. Quero, S. Doerr, and R. Hernández-Clemente, “Determination of forest fuels characteristics in mortality-affected Pinus forests using integrated hyperspectral and ALS data,” *Int. J. Appl. Earth Observ. Geoinf.,* vol. 68, pp. 157–167, 2018.

[94] T. P. Dawson, P. J. Curran, and S. E. Plummer, “LIBERTY—Modeling the effects of leaf biochemical concentration on reflectance spectra,” *Remote Sens. Environ.,* vol. 65, no. 1, pp. 50–60, Jul. 1998.

[95] Y.-B. Cheng, P. J. Zarco-Tejada, D. Riaño, C. A. Rueda, and S. L. Ustin, “Estimating vegetation water content with hyperspectral data for different canopy scenarios: Relationships between AVIRIS and MODIS indexes,” *Remote Sens. Environ.,* vol. 105, no. 4, pp. 354–366, 2006.

[96] A. De Santis, E. Chuvieco, and P. J. Vaughan, “Short-term assessment of burn severity using the inversion of PROSPECT and Geosail models,” *Remote Sens. Environ.,* vol. 113, no. 1, pp. 126–136, 2009.

[97] P. J. Zarco-Tejada *et al.*, “Needle chlorophyll content estimation through model inversion using hyperspectral data from boreal conifer forest canopies,” *Remote Sens. Environ.,* vol. 89, no. 2, pp. 189–199, 2004.

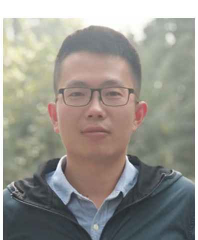

Xingwen Quan received the M.S. degree in cartography and geographic information engineering in 2013 and the Ph.D. degree in information and communication engineering in 2017 from the University of Electronic Science and Technology of China, Chengdu, China.

He is currently an Associate Professor with the School of Environment and Resources, Chengdu, China, and Yangtze Delta Region Institute, Huzhou, China, the University of Electronic Science and Technology of China. His current research focuses on remote sensing of wildfire, including the retrieval of fuel variables (fuel moisture content, fuel load, fuel type, etc.) from remote sensing and their operational application in wildfire danger assessment and early warning.

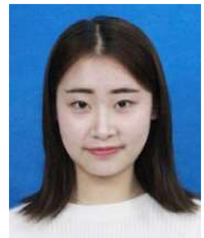

Yanxi Li received the B.S. degree in spatial information and digital technology, in 2018 from the University of Electronic Science and Technology of China, Chengdu, China, where she is currently working toward the Ph.D. degree in information and communication engineering.

Her research interest focuses on remote sensing of forest fuel load and its relationship with wildfire.

Binbin He received the B.S. degree in resource exploration engineering and the M.S. degree in geology from the Chengdu University of Technology, Chengdu, China, in 1996 and 2002, respectively, and the Ph.D. degree in photogrammetry and remote sensing from the China University of Mining and Technology, Xuzhou, China, in 2005.

He is currently a Professor with the School of Environment and Resources, the University of Electronic Science and Technology of China, Chengdu, China. His current research interests include quantitative estimation of land change from satellite remote sensing, and spatiotemporal data mining based on big data.

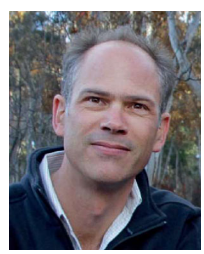

Geoffrey J. Cary received the B.App.Sc. (Hons.) degree in environmental biology from the University of Technology Sydney, Sydney, NSW, Australia, in 1992, and the Ph.D. degree in ecology from The Australian National University, Canberra, ACT, Australia, in 1999.

He is currently an Associate Professor of bushfire science with the Fenner School of Environment and Society, The Australian National University. His research interests include wildland fire simulation, climate change effects on fire regimes, remote sensing of fire fuel, fire ecology from genes to communities, house loss in wildland fire, and laboratory experimentation of fire behavior.

Gengke Lai received the B.S. degree in environmental engineering from the School of Environment and Resources, the University of Electronic Science and Technology of China, Chengdu, China, where he is currently working toward the M.S. degree in surveying and mapping.

His research interests include the optical image processing, the retrieval of vegetation parameters from optical remote sensing images, and the radiative transfer modeling.